Shape and Morphology Effects on the Electronic Structure of TiO$_2$ Nanostructures: From Nanocrystals to Nanorods

Francesca Nunzi,*[,†,‡] Loriano Storchi,[§] Michele Manca,[‖] Roberto Giannuzzi,[‖] Giuseppe Gigli,[‖] and Filippo De Angelis*[,‡]

[†]Dipartimento di Chimica, Biologia e Biotecnologie, Università degli Studi di Perugia, via Elce di Sotto 8, I-06123 Perugia, Italy

[‡]Computational Laboratory of Hybrid/Organic Photovoltaics (CLHYO), Istituto CNR di Scienze e Tecnologie Molecolari, via Elce di Sotto 8, I-06123 Perugia, Italy

[§]Dipartimento di Farmacia, Università G. d'Annunzio, via dei Vestini 31, 66100 Chieti, Italy

[‖]Dipartimento di Matematica e Fisica "E. De Giorgi", Universita' del Salento, Via Arnesano, 73100 Lecce, Italy, and National Nanotechnology Laboratory (NNL)-CNR Istituto Nanoscienze, c/o Distretto Tecnologico, Via Arnesano 16, 73100 Lecce, Italy

(S) Supporting Information

ABSTRACT: We carry out an accurate computational analysis on the nature and distribution of electronic trap states in shape-tailored anatase TiO$_2$ structures, investigating the effect of the morphology on the electronic structure. Linear nanocrystal models up to 6 nm in length with various morphologies, reproducing both flattened and elongated rod-shaped TiO$_2$ nanocrystals, have been investigated by DFT calculations, to clarify the effect of the crystal facet percentage on the nanocrystal electronic structure, with particular reference to the energetics and distribution of trap states. The calculated densities of states below the conduction band

$$g(E_{Fn}) = \frac{\alpha q N_L}{k_B T} exp[\alpha(E_{Fn} - E_C)/k_B T]$$

$\alpha = 0.136$ $\alpha = 0.119$

edge have been very well fitted assuming an exponential distribution of energies and have been correlated with experimental capacitance data. In good agreement with the experimental phenomenology our calculations show that elongated rod-shaped nanocrystals with higher values of the ratio between (100) and (101) facets exhibit a relatively deeper distribution of trap states. Our results point at the crucial role of the nanocrystal morphology on the trap state density, highlighting the importance of a balance between the low-energy (101) and high-energy (100)/(001) surface facets in individual TiO$_2$ nanocrystals.

KEYWORDS: TiO$_2$ nanocrystals, trap states, surface facets, chemical capacitance, DFT
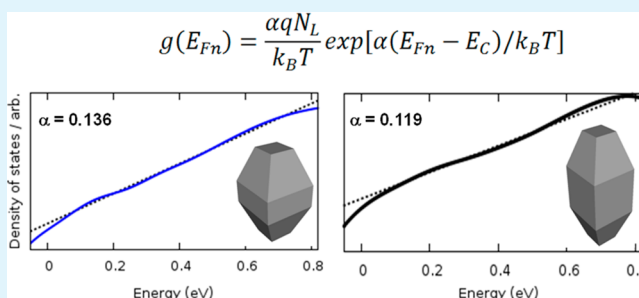
1. INTRODUCTION

Dye-sensitized solar cells (DSCs) represent a promising approach to the direct conversion of sunlight into electrical energy at low cost and high efficiency.[1,2] Compared with traditional inorganic solar cells, DSCs have the peculiarity that the three main functionalities of the solar cell, i.e., the light absorption, the charge carrier separation, and their transport, are fulfilled by different materials, enabling the optimization of each component separately. DSCs are constituted by a dye-sensitized mesoporous oxide layer, typically TiO$_2$, interpenetrated by a liquid redox electrolyte (typically I$^-$/I$_3^-$ or Co(II)/Co(III)−polypyridine complexes in a volatile organic solvent). The photoexcitation of the chemisorbed dye results in injection of an electron in the oxide conduction band (CB) and electron transport through the oxide film to the TCO-coated glass working electrode. The power conversion efficiencies rapidly settled around 10% in the late 1990s, achieving in 2011 a record value of 12.3% employing a zinc-porphyrin dye as sensitizer in conjunction with a cobalt(II/III) as electrolyte.[3] The high surface area of nanoparticulate TiO$_2$ films, while enhancing the dye loading, substantially hinders electron transport through the oxide network, thus limiting the charge-collection efficiency.[4,5] In nanostructured TiO$_2$ films, photoinjected electron transport proceeds by diffusion.[5−8] As a consequence, the electron mobility is more than two orders of magnitude lower than in the corresponding bulk crystals,[7,8] suggesting a high concentration of electron-trapping sites.[9,10] The electronic structure of semiconductor nanoparticles is characterized by CB states (or transport states or extended states), responsible for effective electron transport, and band gap states (or trap states or localized states) that trap and release electrons from and to the CB.[10,11] The investigation of electronic trap states in single crystal and colloidal TiO$_2$ has been the subject of extensive research in the latest ten years.[12−17] A general consensus has been achieved that TiO$_2$ nanocrystals (NCs) show a low-energy tail of localized states below the CB edge.[17−20] In the presence of a broad distribution of localized states, where photoinjected electrons can relax,

electronic transport in mesoporous nanostructured photo-anodes can be described by the multiple-trapping model;[21−26] i.e., it proceeds in an iterative fashion of thermal detrapping, diffusion in the extended CB states, and retrapping. As a result, transport is modulated by electron time in traps. The number and energy depth of traps states is believed to affect the recombination processes of injected photoelectrons with the oxidized dye molecules or the electron acceptors in the electrolyte. Bisquert and coworkers have found that an exponential density of states (DOS) below the CB adequately fits several experimental capacitance data.[14,24] The proposed DOS shape is

$$g(E_{Fn}) = \frac{\alpha q N_L}{k_B T} \exp[\alpha(E_{Fn} - E_C)/k_B T] \tag{1}$$

where q is the electronic charge; N_L is the total number of states below the CB; k_B is the Boltzmann constant; and T is the temperature. E_{Fn} is the Fermi level of the electrons, and α is an adimensional parameter that, together with the conduction band energy edge (E_C), describes the DOS distribution of trap states. Low values of α correspond to a broadening of the density of localized states distribution and are related to a reduction of the trapping phenomena associated with recombination of photogenerated carriers. Typical α values lay in the range 0.2−0.5,[14] although values as small as ∼0.05 have also been reported.[27]

The semiconductor surface plays a crucial role in determining the DSC conversion efficiency since the size and morphology of TiO$_2$ nanoparticles strongly affect the energetics of trap states. The goal is to maintain a high surface area, typical of nanometer-size nanoparticles, while reducing the number of trap states inhibiting the charge collection at the counter electrodes. This can be achieved by realizing photoanodes made of one-dimensional nanocrystalline domains, where an overall reduced number of intergrain defective interfaces can lead to enhanced transport properties.[28,29] However, at relatively large volume one-dimensional nanostructures may be less advantageous in terms of dye adsorption capability, with respect to films constituted by spherical nanoparticles.[30] As predicted by the Wulff construction, the most stable form for anatase NCs is a slightly truncated tetragonal bipyramid,[31] where the (101) surface, being the most thermodynamically stable, is largely predominant over the (001) surface (see Scheme 1). By a careful control of the crystal growth process, shaped-tailored anatase TiO$_2$ NCs with exposed high-energy (001) and (100) facets can be realized. The synthesis of flattened truncated bipyramids in 2008[32] has paved the way to elongated, rod-shaped[33−36] and tetragonal cuboids[37,38] of TiO$_2$ NCs. A recent breakthrough has been the realization of
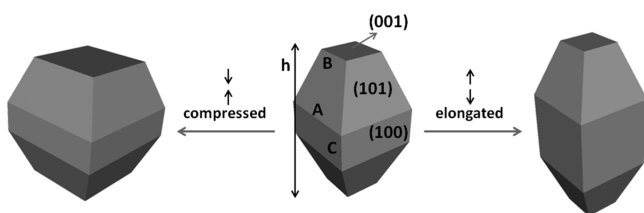
photoelectrodes with mesoporous TiO$_2$ single crystals,[39] showing electron mobilities higher than in conventional TiO$_2$ nanoparticulated photoelectrodes. Photoanodes made of TiO$_2$ one-dimensional nanocrystalline domains with various archi-tectures have been considered to impose preferred electron percolation pathways for photoinjected electrons. Branched morphologies can be considered to enhance the dye loading capacity of the film while still reducing the number of interfaces between TiO$_2$ NCs. Manca et al.[29] analyzed in detail the impact of the morphology of five families of shape-tailored TiO$_2$ anatase NCs on the DSC photovoltaic behavior, namely, three families of linear nanorods (NRs) with variable aspect ratio (AR = 4, 8, 16) and two families of branched NRs with openframework sheaf-like (B) and compact braid-like (BB) morphology (see Table S1 in Supporting Information (SI)). It was found that photoanodes made from linear-shaped NRs with higher AR result in more remarkable downshift of the CB (see Table S1, Supporting Information) that is expected to favor the injection of photogenerated electrons from the LUMO dye. It is however very challenging to disentangle the change in exposed surface area from changes in interparticle contact area when using conventional colloidal NCs, as the exposed surface area of the porous films is inherently related to the crystal size.

Recently, we investigated by quantum mechanical calcu-lations the nature of electronic trap states in individual and sintered realistic anatase TiO$_2$ NCs of ca. 3 nm diameter,[40] pointing out the presence of localized states causing an exponential DOS tail ca. 0.3−0.4 eV below the fully delocalized CB states. In this paper, we move further and employ quantum mechanical DFT and tight-binding DFT (DFTB) calculations to provide an in-depth analysis of the effect of the morphology of realistic shape-tailored anatase TiO$_2$ NCs up to 6 nm in length, on the nature and distribution of the electronic trap states. Starting from the equilibrium shape morphology of TiO$_2$ NCs, we investigated the nature of trap states of elongated rod-shaped and flattened bipyramids, modeling the linear-shaped TiO$_2$ NRs of ref 29. We also considered the effect of branched morphology on the energy and distribution of traps states, by investigating sintered TiO$_2$ NCs assembled with two or three units. Our calculations show that elongated TiO$_2$ NCs, with (100)-rich facets, are characterized by a broadening of the trap density distribution, as testified by a decrease of the α values, in agreement with available experimental trends for NRs of increasing length.

2. COMPUTATIONAL AND EXPERIMENTAL METHODS

To model realistic TiO$_2$ NCs containing up to ca. 3000 atoms, we adopt a multistep computational strategy. We first carry out geometry optimizations by employing self-consistent-charge density-functional tight-binding (SCC-DFTB) methods within the DFTB program.[41,42] We then perform single-point electronic structure calculations on the optimized structures by means of semilocal (i.e., GGA) and nonlocal (i.e., hybrid) DFT within the SIESTA,[43] PWSCF,[44] and ADF[45,46] program packages (see below). Previous works have shown that DFTB can predict band structures, geometrical parameters, and cohesive energies of anatase polymorphs in good agreement with reference DFT and available experimental data.[47,48]

For SIESTA calculations, we employed the GGA-PBE exchange-correlation functional,[49] together with pseudopotentials of the Troullier−Martins type,[50] to model the atomic cores and double-ζ polarization (DZP) basis functions. The semicore 3s and 3p states of Ti were included. A value of 200 meV for the cutoff radius of the confined orbitals and a grid cutoff of 200 Ry have been considered.

Scheme 1. Schematic Drawings of a Single NC in the Equilibrium Truncated Bipyramidal Shape (Middle), a Flattened NC with Rich-(001) Facets (Left), and an Elongated NC with Rich-(100) Facets (Right)

The supercell has been generated automatically in the employed models, allowing negligible interaction between neighboring clusters. SIESTA has shown excellent performances for the calculations of both clusters and periodic systems with a large number of atoms and has also proven to be appropriate for calculations of TiO_2 systems (see for example refs 51−53). For PWSCF calculations, we employed the GGA-PBE exchange-correlation functional,[49] together with ultrasoft pseudopotentials, as implemented in the Quantum Espresso package.[44] Plane-wave basis set cutoffs for the smooth part of the wave functions and the augmented density were 25 and 200 Ry, respectively. A supercell was employed ensuring a minimum separation of 5 Å between periodic images. ADF calculations were performed by employing the hybrid functional B3LYP,[54] together with the double-ζ (DZ) basis set.

To check the accuracy of the GGA DFT approach for the description of the electronic structure of TiO_2 NCs, we compared the GGA-PBE with hybrid B3LYP results with DZ basis set for a $(TiO_2)_{161}-(OH)_3-H_3$ cluster model (see Figure S1 in the SI). As shown in Table S2 in the SI, GGA-PBE and B3LYP give, respectively, a value of 1.68 and 3.59 eV for the energy gap; i.e., the GGA method strongly underestimates the energy gap with respect to the 3.2 eV experimental band gap of anatase, while the hybrid functional overestimates the energy gap, although being more accurate. This result is in agreement with previous theoretical works,[55−57] where the performances of different exchange-correlation functionals on the structural and electronic properties of anatase have been systematically investigated. Indeed it is well known that standard GGA DFT methods underestimate the bulk anatase energy gap, while using alternative approaches, such as hybrid functionals or DFT+U methods,[58−62] a better agreement with experimental data is attained, at the expense of an increased computational cost. Despite the discrepancy in the energy gap values, the DOS for the unoccupied states show very similar features for the two methods (GGA-PBE and hybrid-B3LYP level of theory, see Figure S1 in SI). All the DOS curves have been obtained by a Gaussian convolution of width σ (FWHM = 2.35σ). The DOS curve computed with a hybrid functional is slightly flattened with respect to that computed with the GGA method since the Hartree−Fock exchange contribution tends to increase the amount of localized states at lower energy. To verify the reliability of the GGA approach in the description of the unoccupied states of anatase NCs, we also compare the electron density distribution of the lowest molecular orbitals computed with the GGA-PBE and hybrid B3LYP methods, finding that the composition of the CB is very similar in both cases (see Figure S2 in SI). We can therefore conclude that, even if the GGA approach strongly underestimates the semiconductor energy gap and fails in the description of localized states in reduced bulk anatase,[63] both GGA and hybrid methods deliver almost the same distribution for the electronic states in the CB of anatase NC models. We are therefore confident that the GGA approach is sufficiently accurate for the comparison of unoccupied (both localized and delocalized) states of anatase NCs with different size and shape. We further checked the quality of the PBE/DZP approach, as implemented in SIESTA code, for the electronic structure calculation of the cluster model **1**, by comparing the DOS obtained at the DFTB optimized geometry by DFTB itself, PBE/DZP and PBE/PW levels of theory. The results, Figure S3 in SI, indicate very similar DOS curves for the three methods (the DFTB and PBE/PW curves are essentially indistinguishable). What is most relevant to our study, the shape of the DOS tail is essentially the same in the three cases, despite that the three methods deliver a different band gap for **1** (3.17, 1.91, and 1.68 eV for DFTB, PBE/DZP, and PBE/PW, respectively).

On the basis of the above calibration studies, we have adopted the PBE/DZP method to describe the electronic structure of individual and sintered (two units) NCs, while the less computational intensive DFTB method has been confidently used to study the electronic structure of larger sintered NCs with three units.

Electrochemical impedance spectroscopy (EIS) spectra were recorded using an AUTOLAB PGSTAT302N potentiostat operating in a two-electrode mode. Measurements were carried out both in the dark and under illumination at various forward bias voltages in the 300

kHz to 10 mHz frequency range and applying an AC voltage of 10 mV. Bias potentials ranged from 0.5 to 0.82 V, depending on the open-circuit photopotential of the cell under illumination at 1 sun. The frequency-dependent impedance was fitted by using the Z-view software.

The charge extraction technique was used to estimate the amount of charges stored in the cell under variable working conditions. In particular, cells were kept at open circuit under a given white light intensity supplied using white LEDs (Luxeon, LXML-PWC2). As soon as the LED was switched off, the cell was simultaneously short-circuited, and the resulting discharge current was integrated to calculate the total charge density in the photoelectrode. In this way the recombination loss during charge extraction could be reasonably neglected. The intensity from the LEDS was controlled by varying the current from a Keithley Source Meter 2440. Light intensity was quoted in "sun" equivalents calibrated with a spectrally matched silicon photodiode.

3. RESULTS AND DISCUSSION

3.1. Electrochemical Properties. In Figure 1 we report the plots of the chemical capacitance for the above referenced
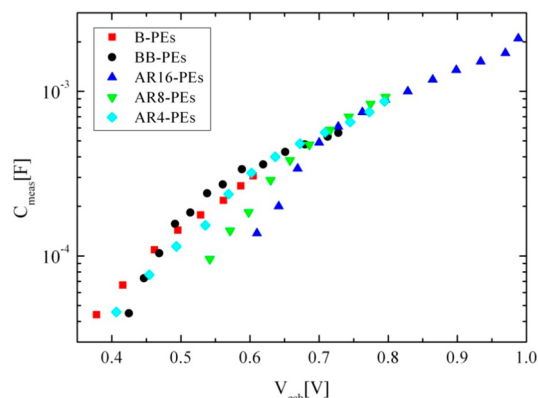

Figure 1. Chemical capacitance of the TiO_2 photoelectrodes for different devices as a function of the equivalent conduction band potential obtained from impedance spectra under 1 sun illumination.

five different breeds of photoelectrodes (PEs) as a function of the equivalent conduction band potential, which helps to visualize the remarkable differences attributable to the contribution of the Helmholtz layer capacitance (which are basically proportional to the surface area) at potentials lower than 0.7 V.

At the lower potentials the measured electrochemical capacitance is dominated by the Helmholtz layer, C_H, and by the adsorbed ionic species, C_{ad}, whereas at higher ones the chemical capacitance of TiO_2, C_μ, governs the capacitive response of the cell.[64] The latter also exhibits an exponential trend as a function of V_{corr},[29] which arises from energetic distribution of the trap state density just below the conduction band edge. Such a distribution is governed by the parameter α ($\alpha = T/T_0$ where T_0 is the characteristic temperature of the distribution) according to[64,65]

$$C_\mu = C_0 \exp\left(\frac{\alpha e}{k_B T} V_{corr}\right) \tag{2}$$

In our case the intimate morphology of the TiO_2 building blocks is determining not only the absolute magnitude of this parameter but also the slope of the logarithmic plot.

C_μ depends on the DOS in TiO_2, $g(E_{Fn})$, according to the following equation[66]

$$C_\mu = L(1 - p)qg(E_{Fn}) \tag{3}$$

where L represents the TiO_2 film thickness; p is its porosity; and $g(E_{Fn})$ is given by eq 1.

Chemical capacitance C_μ thus provides quantitative information about the position of the CB as well as about the value of the band shift (ΔE_c) with respect to a reference electrode. In this work AR4-PE has been assumed as a reference electrode.

Voltage potential at the equivalent conduction band position V_{ecb} can be defined as the following

$$V_{ecb} = V_{corr} - \Delta E_c/q \tag{4}$$

By replacing the expression of V_{corr} from eq 4 into eq 2 it is thus possible to plot the chemical capacitance as a function of V_{ecb} and compare the energetic distributions of the here referred to five TiO_2 films at a fixed value of electron density.

3.2. Structural Properties. We generated the starting NC structures by cleaving bulk anatase TiO_2 according to the typical bipyramidal Wulff shape. The resulting NCs expose (101) surfaces on the lateral facets, (001) surfaces on the truncation facets, and (100) surfaces at the junction of the two pyramids. After verifying the impossibility to generate perfectly crystalline and stoichiometric, $(TiO_2)_n$, truncated bipyramidal NC structures, we build up our models in the following: by saturating on the (001) surfaces (i) all the monocoordinated dangling oxygen atoms by hydrogen atoms and (ii) all the tetracoordinated titanium atoms with OH groups (see Figure 2). With reference to the equilibrium NC bipyramidal shape,
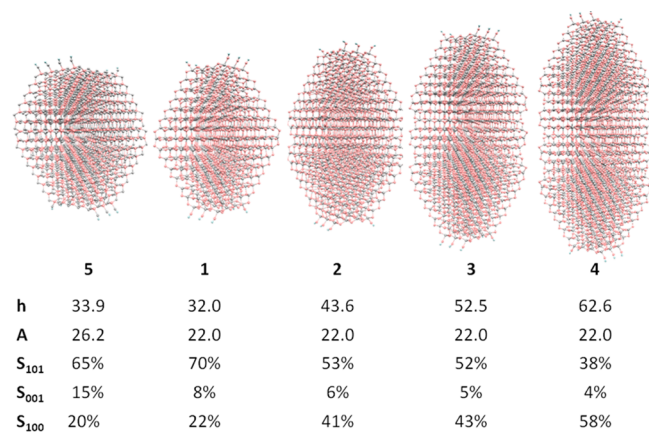

	5	1	2	3	4
h	33.9	32.0	43.6	52.5	62.6
A	26.2	22.0	22.0	22.0	22.0
S_{101}	65%	70%	53%	52%	38%
S_{001}	15%	8%	6%	5%	4%
S_{100}	20%	22%	41%	43%	58%

Figure 2. Optimized geometries for equilibrium-shaped (**1**), elongated rod-shaped (**2–4**), and flattened (**5**) TiO_2 NC models. The main geometrical parameters (h and A, see Scheme 1) are also shown (in Angstrom), together with the facet percentage of the (101), (001), and (100) surfaces. A complete list of the geometrical parameters is reported in Table S1 in the SI.

we considered linear NC models with various morphologies, with length up to 6 nm. Taking into account a $(TiO_2)_{411}-(OH)_6-H_6$ NC (structure **1** in Figure 2) as an equilibrium-shaped structure (B/A = 0.30), we considered three elongated rod-shaped TiO_2 NC structures with increasing (100) surface facets, namely, $(TiO_2)_{580}-(OH)_6-H_6$, **2**, $(TiO_2)_{749}-(OH)_6-H_6$, **3**, and $(TiO_2)_{918}-(OH)_6-H_6$, **4**, and one flattened NC structure, namely, $(TiO_2)_{554}-(OH)_7-H_7$, **5** (see Figure 2). Branched morphologies have been also investigated by sintering NCs in the structure **1**, attaching two or three single crystals through the 101/101 facets (see Figure 3).
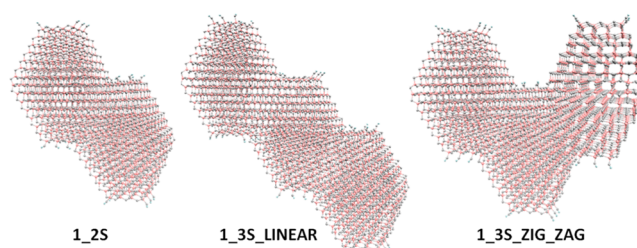

Figure 3. Optimized geometries for two-sintered (**1_2S**, left) and three-sintered (linear **1_3S_LINEAR**, middle, and zig-zag **1_3S_ZIG-ZAG**, left, configuration) NCs, the constituting units being model **1**.

As described in detail in ref 40, the facets of our NC models are characterized by Ti and O atoms undercoordinated with respect to the bulk, where Ti and O atoms have a pseudo-octahedral (Ti_{6c}) and pseudo-trigonal (O_{3c}) coordination, respectively. In particular, for all the considered NC models, five-fold Ti^{4+} (Ti_{5c}) and two-fold coordinated O^{2-} (O_{2c}) sites are present on the (101) and (001) facets, as found on extended surfaces.[67−69] In structure **1**, we also identified four tetracoordinated Ti^{4+} sites (Ti_{4c}) that occur on the vertices at the intersection of the four (101) cleavage planes and give rise to (100) facets, constituting like a belt around the NC square cross-section of the NC. We verified the impossibility to generate NC models without (100) facets that unavoidably arise upon TiO_2 bulk cleavage along the (101) Miller planes; i.e., the undercoordinated Ti_{4c} sites represent an intrinsic characteristic of TiO_2 NCs. In the elongated rod-shaped NC models **2−4** the (100) facet length along the [001] direction increases with respect to **1**, together with the number of the undercoordinated Ti_{4c} sites lying on the (100) facets. For instance, passing from **1** to **4**, the (100) surface percentage is tripled, while the (101) and (100) surface percentages are halved and unaltered, respectively (see Figure 2). Accordingly, in **2**, **3**, and **4** we can distinguish, respectively, two, three, and four belts constituted by (100) facets, each belt involving four undercoordinated Ti_{4c} sites at the vertexes of the NC square cross-section, that are able to act as traps for electrons. The presence of undercoordinated Ti_{4c} sites in the TiO_2 mesoporous films and their correlation with trap states for electronic transport has been the subject of various papers by Teng et al.[70−72] In the flattened NC model **5**, the bipyramid cross-section area has grown along the [010] direction, causing an increase of the A parameter value. In particular, in structure **5** we fix the values of B, C, and h parameter as in **1**, while increasing A from 22 to 26 Å. The net result is a doubling of the (001) surface percentage at the expense of (101) and (100) with respect to the equilibrium shape **1** (see Figure 2 and Table S1 in SI).

Upon geometry optimization of **1−5** NCs, the largest structural distortions with respect to the bulk crystalline structures occur at the Ti_{4c} undercoordinated sites, which rearrange from the undercoordinated octahedral configuration, characteristic of the bulk-truncated structure, to a distorted tetrahedral configuration. This feature is found in all the investigated NC models at all levels of theory employed, thus suggesting that the presence of pseudotetrahedral Ti_{4c} sites is a typical feature of these NC structures. Moreover, the rod-shaped **2−4** NCs with larger (100) exposed facets show a remarkable distortion from the bulk structure, thus suggesting that the inherent electronic trap states will affect strongly the charge carrier transport through the TiO_2 mesoporous film. On

the other hand, NC **5**, retaining almost the same (100) surface percentage of **1**, is expected to possess almost the same distribution of inherent trap states.

To investigate the effect of branched morphologies on the trap state distribution, we also considered sintered NCs, constituted by two (**1_2S**) or three units (**1_3S**) of **1** attached by 101/101 interfaces (see Figure 3), that have been computed as the most effective interactions in our previous study.[40] Upon geometry optimization, the structure of two/three NCs tends to become similar to a bulk structure, thus attaining crystallographic matching with each other. The reconstruction of the sintered NCs is expected to decrease the trapping events in electron transport. A linear (**1_3S_LINEAR**) and a zig-zag (**1_3S_ZIG_ZAG**) configuration has been verified for three units sintered NCs, the former being more stable by 6.2 eV.

3.3. Electronic Properties of Shape-Tailored Individual and Sintered TiO₂ NCs.

The electronic structures of NCs **1**−**5** computed at the PBE/DZP (DFTB) level of theory are compared in terms of density of states (DOS), focusing on the manifold of unoccupied states (see Figure 4 and S4 in SI). For
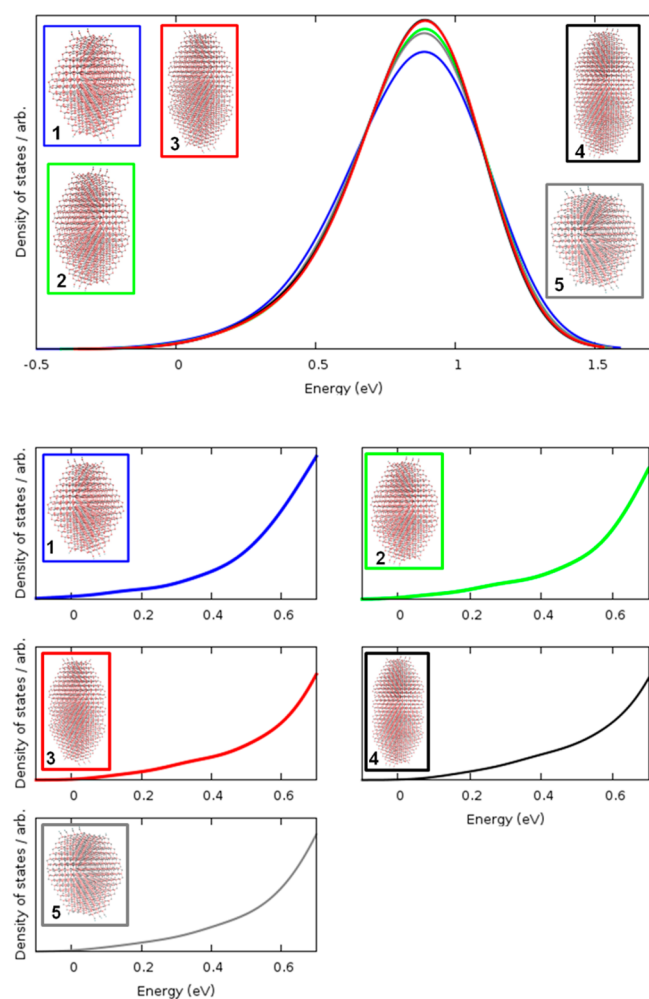

Figure 4. Top of the panel: DOS profile (300 lowest unoccupied states) for models **1**−**5** (also shown as insets) calculated at the DFTB optimized geometry with PBE/DZP level of theory (σ = 0.18 eV). The five DOS have been aligned at their maximum. The zero of the energy is set at the LUMO for each data set. Bottom of the panel: a magnification of the low-energy region up to 0.7 eV from the LUMO of each data set (σ = 0.08 eV).

elongated NCs, we find the band gap values slightly decreasing from 1.91 (3.17) eV in **1** to 1.79 (2.94) in **4**, essentially due to an up-shift and a down-shift in energy of the HOMO and LUMO, respectively, while for the flattened NC **5** the band gap is unaltered with respect to **2** (see Table S3 in SI).

To compare the calculated DOS for TiO₂ NCs with available experimental data from capacitance measurements on dye-sensitized TiO₂,[29] we fitted our data to eq 1 in its logarithmic form. As shown in Figure 5 and Figure S5 in the SI, very good linear fits (R^2 = 0.99) were obtained in an energy range ca. 0.1−0.7 (0.1−0.6) eV above the LUMO. Below 0.1 eV, a few localized states are found, while above 0.7 (0.6) eV the DOS of our models changes its shape and slope due to the finite system's dimension. Also notice that although a Gaussian broadening has been used to calculate the DOS, this should not directly influence the fit, which does not include the tail below the LUMO originated by the broadening. The resulting α and E_c values (cf. eq 1) for NCs **1**−**5** are reported in Figure 5 and Table S6 in the SI (at T = 300 K). For elongated rod-shaped NC models, α values computed at the PBE/DZP (DFTB) level of theory sligtly decrease from 0.136 (0.119) in **1** to 0.119 (0.104) in **4**, in fairly good agreement with the experimental trend observed in ref 29, while the flattened model **5** retains almost the same α value of **2**, i.e., 0.128 (0.104). The α values computed at the DFTB level of theory show a similar trend as the more accurate PBE/DZP calculations (see Table S6 in SI). Although the computed α values are on the lower edge of measured data (0.25−0.33),[29] our calculations correctly reproduce the effect of the NC morphology on the trap state distribution, pointing out a decrease in the α value for NCs with higher AR. However, TiO₂ NCs constituting DSC photoelectrodes[29] have an AR considerably higher with respect to the employed NC models, so that lower α values are reasonably expected from our calculations. A decrease in the α value corresponds to a broadening of the trap state distribution and is related to a reduction of trapping events in electron transport. We also notice that the computed E_c values show a downward energy shift by 0.264 (0.314) eV passing from **1** to **4**, showing that rod-shaped NCs have lower values for E_c. The flattened model **5** shows an E_c equal to −0.308 eV, i.e., a value that is intermediate between **2** and **3**. However, the determination of E_c values strongly depends on the total trap density N_L that is expected to vary, changing the TiO₂ NC morphology (see Table S1, SI), so that the evaluation of the conduction band edge E_c is still arbitrary, while the α values are expected to be less sensitive to the total trap density N_L.

A recent study on the charge carrier transport properties in TiO₂ mesoporous films for photocatalytic applications[73] has shows that a reduction of the charge carrier recombination can be attained by controlling the percentage of the high-energy (100) and (001) facets, acting as oxidation sites, with respect to the more thermodynamically stable (101) facets, acting as reduction sites. An optimum ratio of the surface percentage of adjacent (101) and (100) facets that are likely to trap electrons and holes, respectively, can lead to an optimum pathway length of the photogenerated carriers in TiO₂ NCs and a minimization of the recombination events.[74] The investigated rod-shaped NC models show an increase of the (100) percentage facets at the expense of the thermodynamically most stable (101) percentage facets (see Figure 1 and Table S1, SI). The reduction of trapping events in electron transport for lower α values can be related to the increase of the (100) facets, passing from 22% in **1** to 58% in **4** and allowing a longer lifetime for the
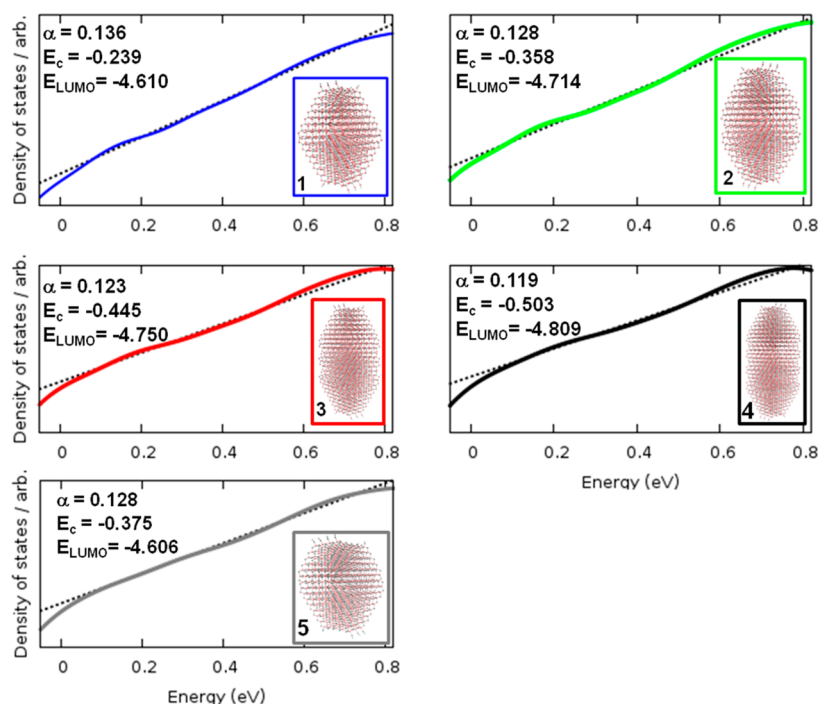
Figure 5. Linear fit $(\ln[g(E_{Fn})] = \ln a + a\cdot(E_{Fn} - b)$, with $a = \alpha$, $b = -E_c$, dotted line) of log data obtained from the DOS (300 lowest unoccupied states, full line) of models **1**−**5** (also shown as insets) calculated at the DFTB optimized geometry with PBE/DZP level of theory ($\sigma = 0.008$ eV). The zero of the energy is set at the LUMO for each data set. E_c and E_{LUMO} are given in eV.

photogenerated electrons. It is worth noting that, despite the high S_{100} percentage of **4** (58%), the α value only slightly decreases, passing from **3** (0.123) to **4** (0.119). This can be due to the low percentage of the (101) surface that has been shown to play a crucial role in the charge transport of TiO_2 NCs.

For all the considered NCs, we find that the unoccupied states of lowest energy, of titanium t_{2g} character, are localized within the central part of the NC (see left panel of Figure 6), mainly lying across the (100) and (101) surfaces. At higher energy, the unoccupied states are progressively more delocalized (right of Figure 6) with the lowest-energy state completely delocalized over the NC structure being found ca. 0.2−0.4 eV above the LUMO, in agreement with both electrochemical and spectroelectrochemical results[10,11] and with the data fit analysis presented above.

The computed DOS for the investigated sintered configurations confirms that the shape of the CB DOS is essentially unaffected by the NC boundaries, due to the almost perfect formation of crystalline domains, while small differences are found in the DOS tail, due to the reconstruction of bulk TiO_2 structure upon saturation of undercoordinated Ti sites. Indeed the calculated α values ($T = 300$ K) for **1** and **1_2S** at the PBE/DZP level of theory (see Figure 7) are almost unaffected by sintering, passing from 0.136 to 0.131. The computed α values ($T = 300$ K) at the DFTB level of theory for three units sintered TiO_2 NCs show essentially the same values of one individual unit (0.119).

4. CONCLUSIONS

We have performed a detailed computational study to investigate the nature and distribution of electronic trap states in shape-tailored anatase TiO_2 NCs, comparing our results to experimental capacitance measurements. Linear NC models with various morphologies, reproducing both flattened and
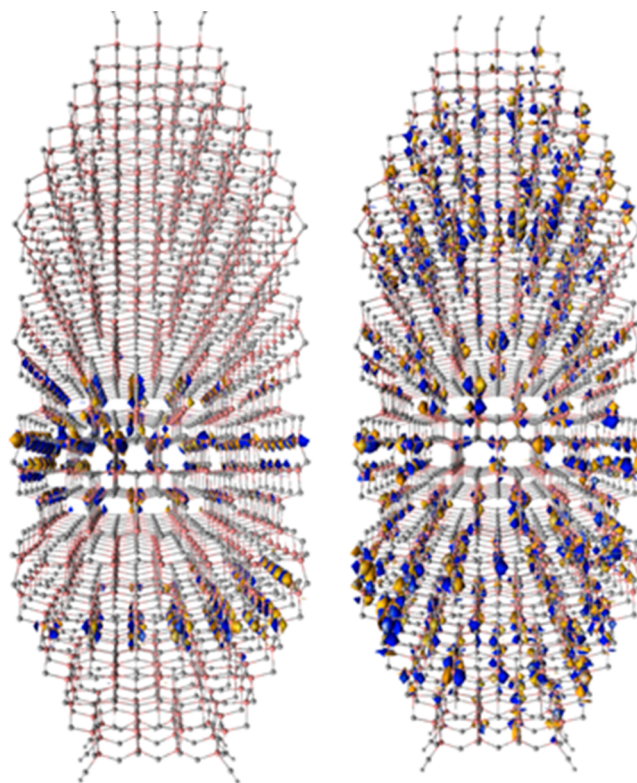

Figure 6. Molecular orbitals of model **4**, representative of localized trap states (left) and delocalized electronic states (right).

elongated rod-shaped TiO_2 NCs, have been investigated with DFT-based methods, attempting to clarify the effect of the crystal facet percentage on the NC electronic structure, with particular reference to the energetics and distribution of trap
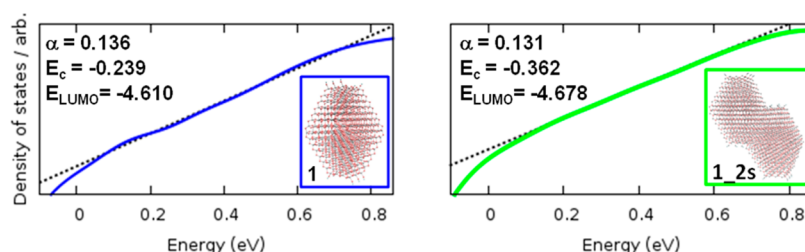
Figure 7. Linear fit $(\ln[g(E_{\mathrm{Fn}})] = \ln a + a \cdot (E_{\mathrm{Fn}} - b)$, with $a = \alpha$, $b = -E_c$, dotted line) of log data obtained from the DOS (300 lowest unoccupied states, full line) of individual (**1**) and sintered NC models (also shown as insets) calculated at the DFTB optimized geometry with PBE/DZP level of theory ($\sigma = 0.008$ eV). The zero of the energy is set at the LUMO for each data set. E_c and E_{LUMO} are given in eV.

states. We also considered the effect of branched morphology on the energy and distribution of traps states, by investigating sintered TiO_2 NCs assembled with two or three units.

The calculated densities of states below the CB edge have been very well fitted to an exponential distribution of states and have been correlated with experimental capacitance data. In agreement with the extrapolated chemical capacitance values, our calculations show that elongated rod-shaped NCs, with lower (101) and higher (100) surface percentage, are characterized by a broadening of the trap density distribution, as testified by a decrease of the α values, so that enhanced photovoltaic performances are expected. It is worth noting that the above referenced energetic considerations have been deduced from DFT calculations conducted on single TiO_2 NC building blocks. However, changes to the surface properties of the photoanodes are usually reflected in the density of sub-bandgap states of the material. DOS of different photo-electrodes reported in ref 29 have been in fact extrapolated from the electrochemical capacitance values measured on the sintered mesostructured film, which implies that a relevant contribution to the determination of number of trap states N_L comes from grain boundaries at the sintering necks, and the number of grain boundaries strongly depends on the size and shape of NCs. In ref 29 the thickness of the film has indeed been kept constant, whereas the total surface area (and hence the total number of necks linking two neighboring NCs) sensitively varied as a function of the intimate morphology of the constituting NRs. CBs were in fact characterized by the minimum number of grain boundaries, and they correspondingly exhibit the lowest value of α (even if the overall aspect ratio is lower than 6). However, recent studies on films with the same morphology but different crystal size showed that the trap density was relatively independent of the density of grain boundaries, suggesting that the morphological dimensions, not grain boundaries, primarily determine the trap density.[75] This supports the consistency of our calculations.

Our study highlights the key role of the fine tuning of the NC morphology for the control of the energetics and distribution of trap states in nanostructured TiO_2 films, aiming to facilitate the electron transport, minimize the recombination losses, and increase the charge-collection efficiency. In particular, our results point to the importance of a balance between the low-energy (101) and high-energy (100)/(001) surface facets in individual TiO_2 NCs to enhance the photoconversion efficiency in DSCs. We believe this study to open the way to the further optimization of different TiO_2 morphologies for photocatalytic and solar cell applications, by establishing the required structure/property relations.

■ ASSOCIATED CONTENT

ⓢ Supporting Information

Main geometrical and electronic parameters for NC models **1**–**5**. DOS profile for NC models **1**–**5** and the $(TiO_2)_{161}$–$(OH)_3$–H_3 model at various levels of theory. Linear fit for NC models **1**–**5** and sintered two- and three-unit NC model **1**. This material is available free of charge via the Internet at http://pubs.acs.org.

■ AUTHOR INFORMATION

Corresponding Authors
*E-mail: nunzi@thch.unipg.it.
*E-mail: filippo@thch.unipg.it.

Notes
The authors declare no competing financial interest.

■ REFERENCES

(1) O'Regan, B.; Grätzel, M. *Nature* **1991**, *353*, 737–740.
(2) Hagfeldt, A.; Boschloo, G.; Sun, L.; Kloo, L.; Pettersson, H. *Chem. Rev.* **2010**, *110*, 6595–6663.
(3) Yella, A.; Lee, H.-W.; Tsao, H. N.; Yi, C.; Chandiran, A. K.; Nazeeruddin, M. K.; Diau, E. W.-G.; Yeh, C.-Y.; Zakeeruddin, S. M.; Grätzel, M. *Science* **2011**, *334*, 629–634.
(4) Bisquert, J.; Cahen, D.; Hodes, G.; Ruhle, S.; Zaban, A. *J. Phys. Chem. B* **2004**, *108*, 8106–8118.
(5) van de Lagemaat, J.; Park, N. G.; Frank, A. J. *J. Phys. Chem. B* **2000**, *104*, 2044–2052.
(6) Bisquert, J. *J. Phys. Chem. B* **2002**, *106*, 325–333.
(7) Cao, F.; Oskam, G.; Meyer, G. J.; Searson, P. C. *J. Phys. Chem.* **1996**, *100*, 17021–17027.
(8) Dloczik, L.; Ileperuma, O.; Lauermann, I.; Peter, L. M.; Ponomarev, E. A.; Redmond, G.; Shaw, N. J.; Uhlendorf, I. *J. Phys. Chem. B* **1997**, *101*, 10281–10289.
(9) Bailes, M.; Cameron, P. J.; Lobato, K.; Peter, L. M. *J. Phys. Chem. B* **2005**, *109*, 15429–15435.
(10) Zaban, A.; Greenshtein, M.; Bisquert, J. *Chem. Phys. Chem.* **2003**, *4*, 859–864.
(11) Bisquert, J.; Zaban, A.; Greenshtein, M.; Mora-Seró, I. *J. Am. Chem. Soc.* **2004**, *126*, 13550–13559.
(12) Ardo, S.; Meyer, G. J. *Chem. Soc. Rev.* **2009**, *38*, 115–164.
(13) Thompson, T. L.; Yates, J. T. *Chem. Rev.* **2006**, *106*, 4428–4453.
(14) Fabregat-Santiago, F.; Garcia-Belmonte, G.; Mora-Sero, I.; Bisquert, J. *Phys. Chem. Chem. Phys.* **2011**, *13*, 9083–9118.
(15) Bisquert, J. *Phys. Chem. Chem. Phys.* **2008**, *10*, 49–72.
(16) Westermark, K.; Henningsson, A.; Rensmo, H.; Sodergren, S.; Siegbahn, H.; Hagfeldt, A. *Chem. Phys.* **2002**, *285*, 157–165.

(17) Barnes, P. R. F.; Miettunen, K.; Li, X.; Anderson, A. Y.; Bessho, T.; Gratzel, M.; O'Regan, B. C. *Adv. Mater.* **2013**, *25*, 1881−1922.

(18) Berger, T.; Sterrer, M.; Diwald, O.; Knözinger, E.; Panayotov, D.; Thompson, T. L.; Yates, J. T. *J. Phys. Chem. B* **2005**, *109*, 6061−6068.

(19) Peter, L. M.; Duffy, N. W.; Wang, R. L.; Wijayantha, K. G. U. *J. Electroanal. Chem.* **2002**, *524*, 127−136.

(20) Kopidakis, N.; Neale, N. R.; Zhu, K.; van de Lagemaat, J.; Frank, A. J. *Appl. Phys. Lett.* **2005**, *87*, 202106−202108.

(21) de Jongh, P. E.; Vanmaekelbergh, D. *Phys. Rev. Lett.* **1996**, *77*, 3427−3430.

(22) Durrant, J. R.; Haque, S. A.; Palomares, E. *Coord. Chem. Rev.* **2004**, *248*, 1247−1257.

(23) Bisquert, J. *J. Electroanal. Chem.* **2010**, *646*, 43−51.

(24) Bisquert, J. *Phys. Chem. Chem. Phys.* **2008**, *10*, 3175−3194.

(25) Barzykin, A. V.; Tachiya, M. *J. Phys. Chem. B* **2002**, *106*, 4356−4363.

(26) Durrant, J. R. *J. Photochem. Photobiol. A: Chem.* **2002**, *148*, 5−10.

(27) Jennings, J. R.; Ghicov, A.; Peter, L. M.; Schmuki, P.; Walker, A. B. *J. Am. Chem. Soc.* **2008**, *130*, 13364−13372.

(28) Jiu, J.; Isoda, S.; Wang, F.; Adachi, M. *J. Phys. Chem. B* **2006**, *110*, 2087−2092.

(29) Agosta, R.; Giannuzzi, R.; De Marco, L.; Manca, M.; Belviso, M. R.; Cozzoli, P. D.; Gigli, G. *J. Phys. Chem. C* **2013**, *117*, 2574−2583.

(30) Ghadiri, E.; Taghavinia, N.; Zakeeruddin, S. M.; Gratzel, M.; Moser, J. E. *Nano Lett.* **2010**, *10*, 1632−1638.

(31) Diebold, U. *Surf. Sci. Rep.* **2003**, *48*, 53−229.

(32) Yang, H. G.; Sun, C. H.; Qiao, S. Z.; Zou, J.; Liu, G.; Smith, S. C.; Cheng, H. M.; Lu, G. Q. *Nature* **2008**, *453*, 638−641.

(33) Zhao, J.; Zou, X.-X.; Su, J.; Wang, P.-P.; Zhou, L.-J.; Li, G.-D. *Dalton Trans.* **2013**, *42*, 4365−4368.

(34) Li, J.; Xu, D. *Chem. Commun.* **2010**, *46*, 2301−2303.

(35) Pan, J.; Wu, X.; Wang, L.; Liu, G.; Lu, G. Q.; Cheng, H.-M. *Chem. Commun.* **2011**, *47*, 8361−8363.

(36) Dinh, C.-T.; Nguyen, T.-D.; Kleitz, F.; Do, T.-O. *ACS Nano* **2009**, *3*, 3737−3743.

(37) Zhao, X.; Jin, W.; Cai, J.; Ye, J.; Li, Z.; Ma, Y.; Xie, J.; Qi, L. *Adv. Funct. Mater.* **2011**, *21*, 3554−3563.

(38) Lai, Z.; Peng, F.; Wang, Y.; Wang, H.; Yu, H.; Liu, P.; Zhao, H. *J. Mater. Chem.* **2012**, *22*, 23906−23912.

(39) Crossland, E. J. W.; Noel, N.; Sivaram, V.; Leijtens, T.; Alexander-Webber, J. A.; Snaith, H. J. *Nature* **2013**, *495*, 215−219.

(40) Nunzi, F.; Mosconi, E.; Storchi, L.; Ronca, E.; Selloni, A.; Grätzel, M.; De Angelis, F. *Energy Environ. Sci.* **2013**, *6*, 1221−1229.

(41) Elstner, M.; Porezag, D.; Jungnickel, G.; Elsner, J.; Haugk, M.; Frauenheim, T.; Suhai, S.; Seifert, G. *Phys. Rev. B* **1998**, *58*, 7260−7268.

(42) Aradi, B.; Hourahine, B.; Frauenheim, T. *J. Phys. Chem. A* **2007**, *111*, 5678−5684.

(43) Soler, J. M.; Artacho, E.; Gale, J. D.; Garcia, A.; Junquera, J.; Ordejon, P.; Sanchez-Portal, D. *J. Phys.: Condens. Matter* **2002**, *14*, 2745−2779.

(44) Giannozzi, P.; Baroni, S.; Bonini, N.; Calandra, M.; Car, R.; Cavazzoni, C.; Ceresoli, D.; Chiarotti, G. L.; Cococcioni, M.; Dabo, I. *J. Phys.: Condens. Matter* **2009**, *21*, 395502.

(45) te Velde, G.; Bickelhaupt, F. M.; Baerends, E. J.; Guerra, C. F.; Van Gisbergen, S. J. A.; Snijders, J. G.; Ziegler, T. *J. Comput. Chem.* **2001**, *22*, 931−967.

(46) Guerra, C. F.; Snijders, J. G.; te Velde, G.; Baerends, E. J. *Theor. Chem. Acc.* **1998**, *99*, 391−403.

(47) Dolgonos, G.; Aradi, B.; Moreira, N. H.; Frauenheim, T. *J. Chem. Theory Comput.* **2010**, *6*, 266−278.

(48) Fox, H.; Newman, K. E.; Schneider, W. F.; Corcelli, S. A. *J. Chem. Theory Comput.* **2010**, *6*, 499−507.

(49) Perdew, J. P.; Burke, K.; Ernzerhof, M. *Phys. Rev. Lett.* **1996**, *77*, 3865−3868.

(50) Troullier, N.; Martins, J. L. *Phys. Rev. B* **1991**, *43*, 8861−8869.

(51) Li, Y.-F.; Liu, Z.-P. *J. Am. Chem. Soc.* **2011**, *133*, 15743−15752.

(52) Sánchez-de-Armas, R. o.; Oviedo López, J. A.; San-Miguel, M.; Sanz, J. F.; Ordejón, P.; Pruneda, M. *J. Chem. Theory Comput.* **2010**, *6*, 2856−2865.

(53) He, T.; Hu, Z. S.; Li, J. L.; Yang, G. W. *J. Phys. Chem. C* **2011**, *115*, 13837−13843.

(54) Stephens, P. J.; Devlin, F. J.; Chabalowski, C. F.; Frisch, M. J. *J. Phys. Chem.* **1994**, *98*, 11623−11627.

(55) Zhang, Y. F.; Lin, W.; Li, Y.; Ding, K. N.; Li, J. Q. *J. Phys. Chem. B* **2005**, *109*, 19270−19277.

(56) Lazzeri, M.; Vittadini, A.; Selloni, A. *Phys. Rev. B* **2001**, *63*, 155409.

(57) Martsinovich, N.; Jones, D. R.; Troisi, A. *J. Phys. Chem. C* **2010**, *114*, 22659−22670.

(58) Finazzi, E.; Di Valentin, C.; Pacchioni, G.; Selloni, A. *J. Chem. Phys.* **2008**, *129*, 154113.

(59) Hu, Z.; Metiu, H. *J. Phys. Chem. C* **2011**, *115*, 5841−5845.

(60) Morgan, B. J.; Watson, G. W. *Surf. Sci.* **2007**, *601*, 5034−5041.

(61) Morgan, B. J.; Watson, G. W. *J. Phys. Chem. C* **2009**, *113*, 7322−7328.

(62) Calzado, C. J.; Hernandez, N. C.; Sanz, J. F. *Phys. Rev. B* **2008**, *77*, 045118.

(63) Finazzi, E.; Di Valentin, C.; Pacchioni, G.; Selloni, A. *J. Chem. Phys.* **2008**, *129*, 154113.

(64) Wang, Q.; Ito, S.; Gratzel, M.; Fabregat-Santiago, F.; Mora-Sero, I.; Bisquert, J.; Bessho, T.; Imai, H. *J. Phys. Chem. B* **2006**, *110*, 25210−25221.

(65) Fabregat-Santiago, F.; Randriamahazaka, H.; Zaban, A.; Garcia-Canadas, J.; Garcia-Belmonte, G.; Bisquert, J. *Phys. Chem. Chem. Phys.* **2006**, *8*, 1827−1833.

(66) Barea, E. M.; Ortiz, J.; Paya, F. J.; Fernandez-Lazaro, F.; Fabregat-Santiago, F.; Sastre-Santos, A.; Bisquert, J. *Energy Environ. Sci.* **2010**, *3*, 1985−1994.

(67) Vittadini, A.; Selloni, A.; Rotzinger, F. P.; Grätzel, M. *Phys. Rev. Lett.* **1998**, *81*, 2954.

(68) Selloni, A. *Nat. Mater.* **2008**, *7*, 613−615.

(69) Gong, X. Q.; Selloni, A. *J. Phys. Chem. B* **2005**, *109*, 19560−19562.

(70) Hsiao, P.-T.; Teng, H. *J. Am. Ceram. Soc.* **2009**, *92*, 888−893.

(71) Hsiao, P.-T.; Tung, Y.-L.; Teng, H. *J. Phys. Chem. C* **2010**, *114*, 6762−6769.

(72) Liou, Y.-J.; Hsiao, P.-T.; Chen, L.-C.; Chu, Y.-Y.; Teng, H. *J. Phys. Chem. C* **2011**, *115*, 25580−25589.

(73) Roy, N.; Sohn, Y.; Pradhan, D. *ACS Nano* **2013**, *7*, 2532−2540.

(74) Liu, C.; Han, X. G.; Xie, S. F.; Kuang, Q.; Wang, X.; Jin, M. S.; Xie, Z. X.; Zheng, L. S. *Chem. Asian J.* **2013**, *8*, 282−289.

(75) Docampo, P.; Guldin, S.; Steiner, U.; Snaith, H. J. *J. Phys. Chem. Lett.* **2013**, *4*, 698−703.

2478

dx.doi.org/10.1021/am404293x | *ACS Appl. Mater. Interfaces* 2014, 6, 2471−2478